Journal of Materials Chemistry A

ROYAL SOCIETY OF CHEMISTRY

PAPER

View Article Online
View Journal | View Issue

Check for updates

Cite this: J. Mater. Chem. A, 2023, 11, 10213

Ultralow thermal conductivity in the mixed-anion solid solution $Sn_2SbS_{2-x}Se_xI_3$†

Justin Mark, ‡[a] Wenhao Zhang, ‡[ab] Kazuhiko Maeda, [cf] Takafumi Yamamoto, [d] Hiroshi Kageyama [e] and Takao Mori *[ab]

The mixed-anion compounds $Sn_2SbS_{2-x}Se_xI_3$ (x = 0, 0.2, 0.5) and $Sn_2BiS_2I_3$ were synthesized and characterized. Rietveld refinement, elemental analysis, and diffuse reflectance measurements indicate successful substitution of Se for S and potential for bandgap tunability. Thermal conductivity measurements reveal ultralow thermal conductivities as low as 0.22 W m^{-1} K^{-1} at 573 K within this family of compounds. Such exceptionally low thermal conductivities are anomalous when compared to the previously reported heavier $Pb_2BiS_2I_3$ (0.7 W m^{-1} K^{-1}). Computational analysis in the form of electron localization function and Grüneisen parameter reveal Sn to be the most influential factor that controls the lattice thermal conductivity, due to its localized antibonding electrons and large contribution to structural anharmonicity.

Received 2nd February 2023
Accepted 20th April 2023

DOI: 10.1039/d3ta00609c

rsc.li/materials-a

1 Introduction

In the past, materials design has focused largely on cation substitutions, resulting in structure types often containing multiple cations. Materials design focusing on multiple anions and structure–property trends in these mixed-anion materials is far less established, despite mixed-anion materials providing a large platform for materials design.[1–4] For example, substituting an octahedrally coordinated metal for another metal results in similar metal octahedra which will serve as the building block for a solid-state structure. However, with anion substitutions the options in coordination polyhedra are much more varied, such as *cis*-, *trans*-, *fac*-, or *mer*-octahedra.[1,3] This allows for a variety of structural building blocks which can influence materials properties in unexpected ways. Not only are the coordination environments varied, but a degree of polar distortion can also be introduced to the metal polyhedral building blocks due to the differing electronegativities of the anions, adding another tunable variable to the material design process.[1,3]

The diverse structures of mixed-anion materials remain relatively under explored compared to single anion compounds, however, they have shown to be promising for energy applications. The irregular coordination polyhedra of mixed-anion materials have shown to be reliable building blocks for novel noncentrosymmetric materials, a prerequisite for second harmonic generation, as seen in $Ba_2[GaF_4(IO_3)_2](IO_3)$, $BaGeOSe_2$, and $Sr_3Ge_2O_4Se_3$.[5–7] Other examples of intriguing mixed-anion applications include ionic conductors and thermoelectrics. $Na_2(CB_9H_{10})(CB_{11}H_{12})$ demonstrates significantly improved ionic conductivity compared to the single anion parent compounds, reaching conductivities 7× greater than the well-known superionic conductor $Li_{10}GeP_2S_{12}$, while BiCuSeO is a promising thermoelectric material with ultralow thermal conductivity achieving zT values > 1.[8–12]

Despite the promising properties and diverse structural opportunities in mixed anion materials, most work is reported for oxygen containing materials (oxyhalides, oxychalcogenides, *etc.*).[1,3] However, a recent computational work has shown non-oxide mixed anion materials can exhibit a much more diverse set of crystal structures. This is attributed to the high bond strength of metal-oxide bonds which limit variability compared to those of sulfides, tellurides, *etc.*[13] Thus, we seek to expand on the structure–property relationships in non-oxide mixed anion materials for future materials design.

Given the complexity which can arise in mixed-anion crystal structures, they can serve as a promising platform for low thermal conductivity materials. Indeed, some of the studied mixed-anion materials such as $Pb_2BiS_2I_3$, BiCuSeO, and $Bi_4O_4SeCl_2$ have exhibited exceptionally low thermal conductivities of

[a]International Center for Materials Nanoarchitectonics (WPI-MANA), National Institute for Materials Science (NIMS), Tsukuba, Ibaraki 305-0044, Japan. E-mail: MORI.Takao@nims.go.jp

[b]Graduate School of Pure and Applied Science, University of Tsukuba, Tsukuba, Ibaraki 305-8671, Japan

[c]Department of Chemistry, School of Science, Tokyo Institute of Technology, Tokyo, Japan

[d]Laboratory for Materials and Structures, Institute of Innovative Research, Tokyo Institute of Technology, Yokohama, Japan

[e]Graduate School of Engineering, Kyoto University, Kyoto, Japan

[f]Living Systems Materialogy (LiSM) Research Group, International Research Frontiers Initiative (IRFI), Tokyo Institute of Technology, 4259 Nagatsuta-cho, Midori-ku, Yokohama, Kanagawa, 226-8502, Japan

† Electronic supplementary information (ESI) available. See DOI: https://doi.org/10.1039/d3ta00609c

‡ J. M. and W. Z. contributed equally to this work.

0.7 W m^{-1} K^{-1}, 0.5 W m^{-1} K^{-1}, and 0.1 W m^{-1} K^{-1} respectively.[9,14,15] Thermal conductivity can be divided into two components, electronic (κ_e) and lattice (κ_l) thermal conductivities. The reduction of thermal conductivity by extrinsic methods has been extensively studied as it is easier to manipulate κ_l by extrinsic methods, for example, by various nano–microstructuring[16–18] and/or introducing various defects.[19–22] However, intrinsic thermal conductivity is closely related to the crystal structure and bonding, making it much more difficult to pinpoint and modify. Commonly, heavy elements in a complex crystal structure can lead to complex phonon branching, small phonon velocities and high rates of phonon–phonon scattering, all of them beneficial for achieving lower lattice thermal conductivity.[23] Other structural factors, such as a large interatomic space, weak bonding, partial occupancy, and bonding heterogeneity can provide sources of lattice anharmonicity, further reducing the thermal conductivity.[24–27]

With these factors in mind, we consider the large family of non-oxide mixed-anion $Tt_2PnCh_2I_3$ (Tt = Sn, Pb; Pn = Sb, Bi; Ch = S, Se) compounds for which thermal conductivity is only reported for $Pb_2BiS_2I_3$.[14,28–30] In general they can be described as van der Waals layered compounds with I atoms loosely bonded as bridging atoms within the inter-layer space. Site symmetry is mostly low, indicating potentially large anharmonicity. Furthermore, the large polarizability of iodine can be expected to introduce additional bonding dynamics and reduce lattice thermal conductivity.[31] These interesting structural features and the relative lack of experimental results give us the motivation to investigate into these compounds.

2 Experimental section

2.1 Synthesis

The starting materials, Sn shot (Wako, 99.9%), Sb powder (Sigma-Aldrich, 99.5%), S flakes (Sigma-Aldrich, 99.99%) Se shot (Alfa Aesar, 99.999%), Bi granules (5N Plus Inc., 99.999%), and I_2 beads (Wako, 99.8%) were used as received. Stoichiometric amounts of the elements were loaded into silica ampoules and flame sealed under vacuum. The ampoules were placed in a muffle furnace and heated to 923 K over 12 h and annealed at this temperature for 36 h before allowing the furnace to naturally cool to room temperature. The resulting products are silvery looking ingots which were subsequently ground with a mortar and pestle before further use.

2.2 Powder X-ray diffraction

Powder X-ray diffraction was performed using a Rigaku SmartLab3 with Cu-K_α radiation and operating at 40 kV and 40 mA. Sample powder was prepared using a well holder and compacted using a glass slide. Diffraction patterns were collected in the 2θ range of 5–80° with a step size of 0.01° and scan rate of 2° per minute. Rietveld refinement was performed using the GSAS-II software package.[32]

2.3 SEM-EDS

Elemental analysis of samples was performed using a FE-SEM SU8000 (Hitachi) equipped with a Quantax FQ5060 EDS detector (Bruker). Measurements were performed on polished pieces of sintered pellets mounted on carbon tape and sputtered for 30 s with a carbon coating. Bulk compositions were determined using an average of 3 spots.

2.4 UV/vis spectroscopy

UV/vis diffuse reflectance spectra were collected using a V-770 UV-vis/NIR spectrophotometer equipped with an integrating sphere (JASCO) in the range of 500–2500 nm. Samples were finely ground into powder with a mortar and pestle and pressed against a glass slide for measurements. Data was then converted using the Kubelka–Munk function to determine the bandgap.

2.5 Spark plasma sintering (SPS)

High density pellets of 10 mm diameter were sintered using a SPS-1080 (SPS SYNTEX Inc.). Finely ground powders were loaded into a graphite die between graphite foil and graphite plungers. The pellets were sintered by heating to 573 K over 5 minutes and annealing at this temperature for 5 minutes, all under an argon atmosphere and a uniaxial pressure of 76 MPa. After sintering, pellets were removed from the graphite die and polished to remove traces of graphite. The geometrical density of the resulting pellets was found to be ~96% of their theoretical density.

2.6 Thermal transport properties

For thermal diffusivity measurements samples were cut into disks of 10 mm diameter with a thickness of approximately 1.5 mm. The thermal diffusivity and specific heat were measured under a nitrogen atmosphere using a Laser Flash Analyzer (LFA) 467 Hyperflash (NETZSCH) and a Pyroceram standard in the temperature range of 303–573 K. The thermal conductivity (k) was then determined by the equation $k = \rho D C_p$ where ρ, D, and C_p are the sample density, thermal diffusivity, and specific heat, respectively. Three shots were measured at each temperature and the average values are shown in this work. Low temperature thermal conductivity was measured from 6.5 to 300 K using the thermal transport option (TTO) of a Physical Property Measurement System (PPMS, Quantum Design). For the TTO measurement, we used the four-probe lead configuration with a bar shaped sample (2 mm × 2 mm × 8 mm, parallel to the sintering direction) and thermal conductivity was measured automatically in the continuous mode. We used an emissivity of 1.0 to correct the strong radiation heat loss occurring above 150 K.

2.7 Quantum chemical calculations

The electronic structure of the compounds was calculated self-consistently using density functional theory (DFT) with plane waves, as implemented in the Quantum Espresso (QE) package.[33] We used the generalized gradient approximation (PBE-GGA) pseudopotential in the projector augmented-wave (PAW) method.[34,35] Considering the large interatomic

distances presented in the layered structure, we employed a non-local correction for the van der Waals interaction (vdW-DF).[36] A cutoff of 140 Ry and 1120 Ry was used for the kinetic energy and charge density, respectively, and *k*-grid sampling was done using a grid of 7 × 3 × 6 in the Brillouin zone of the primitive cell. Bader's charge analysis was performed using the Bader code.[37] Electron localization function calculation and wave function projection was performed within QE. VESTA was used for visualization.

For the phonon calculation, we relaxed the structure until the force on each atom is smaller than 1.5×10^{-5} Ry bohr^{-1}. Interatomic force for the phonon calculation was extracted using the frozen phonon method as implemented in the phonopy packages.[38] A displacement of 0.015 Å was used to generate the displacement pattern in a 4 × 1 × 3 supercell with 384 atoms. Reciprocal space was sampled using Γ point only when calculating the force.

3 Result and discussion

3.1 Crystal structure determination

Within the $Tt_2PnCh_2I_3$ (Tt = Sn, Pb; Pn = Sb, Bi; Ch = S, Se) family, there are four different reported structural configurations.[14,28,29] In the 80's $Sn_2SbS_2I_3$ was reported to crystallize in the *Cmcm* space group, based on experiments performed at 293 K and 173 K (Fig. 1a).[29] In 2007, Doussier *et al.* reported the crystal structure of $Pb_2SbS_2I_3$ at 293 K to crystallize in the *Cmcm* space group similar to $Sn_2SbS_2I_3$, but the Sb position for $Sn_2SbS_2I_3$ is occupied by Pb in $Pb_2SbS_2I_3$, while the Sn site is split into two partially occupied overlapping Pb and Sb sub-positions (Fig. 1c).[28] Further experiments at 100 K found the structure to crystallize in the $P2_1/c$ space group with distinct separate Pb and Sb sites (Fig. 1d).[28] The room temperature (RT) and low temperature (LT) phases have similar structures; however, the LT phase eliminates the observed disorder in the RT structure. Using these structure models and bond valence analysis, Doussier *et al.* suggest that the reported $Sn_2SbS_2I_3$ structure to be in error and crystallographic elemental assignments should be similar to $Pb_2SbS_2I_3$.[28,29] Furthermore, Islam *et al.* more recently reported a fourth structural arrangement for $Pb_2BiS_2I_3$ and $Sn_2BiS_2I_3$ at 293 K (Fig. 1b). This crystal structure is nearly identical to that of RT $Pb_2SbS_2I_3$, but the original split crystallographic sites are resolved as single atom positions.[14] Note that the $P2_1/c$ space group is a subgroup of *Cmcm*. This group–subgroup relation can be described by a translationengleich of index 2 (t2) followed by a klassengleich of index 2 (k2), as seen in Fig. S6.†[39,40] This relationship is represented by the following cell transformation:

$$\begin{pmatrix} a \\ b \\ c \end{pmatrix}_{P2_1/c} = \begin{pmatrix} -1/2 & -1/2 & 0 \\ 0 & 0 & 1 \\ 2 & 0 & 0 \end{pmatrix} \begin{pmatrix} a \\ b \\ c \end{pmatrix}_{Cmcm}$$

The difficulty in experimental crystal structure determination mainly arises from the fact that X-ray scattering factors of Sn and Sb (or Pb and Bi) are nearly identical, making their atomic positions ambiguous and difficult to be truly distinguished by X-ray diffraction. However, the crystal structure is of crucial importance for our later theoretical analysis. Therefore, we attempted to determine the stability of the different possible crystal structures for $Sn_2SbS_2I_3$ by comparing the energy of different relaxed structural models from first principles calculation. The structural models were chosen so that they do not include mixed occupancies ($Pb_2SbS_2I_3$ LT) or split sites (reducing the split sites to fixed position), which are difficult to treat in DFT calculations. The key point here is the determination of the positions of Sn and Sb. We considered three models: (1) the original *Cmcm* structure with the split Sb reduced from a half occupied 8f to a fully occupied 4c site, (2) a $P2_1/c$ (lower) symmetry structure with staggered occupancy of the 8f Sb site and (3) the LT-$P2_1/c$ configuration of $Pb_2SbS_2I_3$, reported by Doussier *et al.* with a $Sn_2SbS_2I_3$ composition.[28] We denote them as *Cmcm*-4c, $P2_1/c$-(*Cmcm*), and LT-$P2_1/c$, respectively. The *Cmcm*-4c and $P2_1/c$-(*Cmcm*) are derived from the reported *Cmcm* structure of $Sn_2SbS_2I_3$ but treat the split of the Sb 8f sites in different ways, while LT-$P2_1/c$ represents the configuration in which half the Sn positions are swapped with the Sb position compared to the reported structure. Atomic positions and the lattice parameters for each structure model were optimized using variable-cell optimization routine implemented in Quantum Espresso while keeping the symmetry unchanged. The three crystal structures considered, structure parameters and their respective phonon dispersion are shown in Fig. S7, S8 and Table S2.† We found the *Cmcm*-4c structure is dynamically unstable with the appearance of imaginary phonon modes occurring at most parts of the Brillouin zone, while the two structures in $P2_1/c$ are dynamically stable. DFT calculations of the ground state energies shows that LT-$P2_1/c$ has the lowest energy, with $P2_1/c$-(*Cmcm*) and *Cmcm*-4c being 0.38 eV and 0.64 eV higher per formula unit, respectively. The calculation results agree with the bond valence analysis given by the previous report.[28] With these results, we propose that $Sn_2SbS_2I_3$ shares the same $P2_1/c$ structure as $Pb_2SbS_2I_3$ in its ground state (Fig. 1d) and use it for our later theoretical calculations.

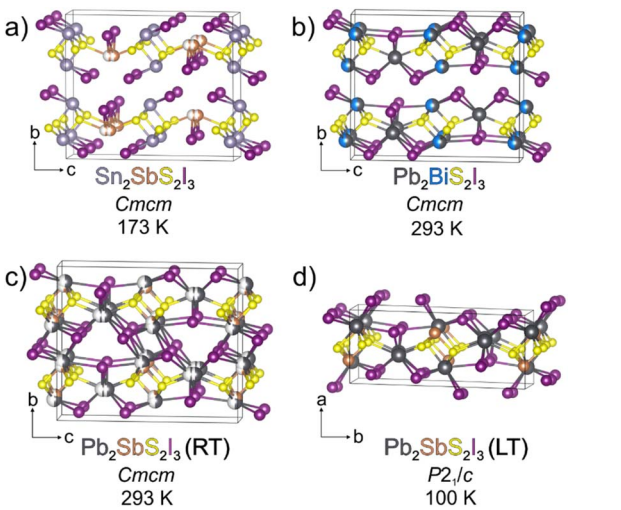

Fig. 1 Reported crystal structures of (a) $Sn_2SbS_2I_3$, (b) $Pb_2BiS_2I_3$, and (c and d) $Pb_2SbS_2I_3$. Crystal structure configuration in (d) is the theoretically determined structure configuration for $Sn_2SbS_2I_3$.

3.2 Experimental synthesis

The solid-state synthesis of $Sn_2SbS_2I_3$ was performed similarly to the procedure reported by Starosta *et al.*[41] As the measured properties within this family of compounds are scarce, in order to build upon the structure–property relationships in these mixed-anion materials, we also attempted to synthesize the reported isostructural $Sn_2SbSe_2I_3$ for comparison of anion effects.[29] However, the synthesis was heavily contaminated with the competing $Sn_3SbSe_2I_5$ phase, thus we resorted to partial Se substituted $Sn_2SbS_2I_3$ for comparison and extrapolation of the $Sn_2SbSe_2I_3$ phase.[29] A series of samples of $Sn_2SbS_{2-x}Se_xI_3$ ($x = 0$, 0.2, 0.5) were synthesized and are discussed herein. Note that attempts to synthesize the $Sn_2SbSSeI_3$ composition began to form significant amounts of undesired side phases.

Powder X-ray diffraction indicates the three sample compositions are nearly identical and match well with the theoretical pattern of $Sn_2SbS_2I_3$ (Fig. 2a). Upon closer comparison of the three experimental patterns, small peak shifts are observed for certain peaks in the direction of lower 2θ with increasing Se content. This indicates an expansion of the unit cells, consistent with the substitution of the larger Se in place of S. Furthermore, the magnitude of the peak shift is strongly correlated to the l index as observed in Fig. 2b, indicating the unit cell expansion is predominantly along the crystallographic c-axis. Rietveld refinement and determined unit cell parameters are shown in Fig. S1 and Table S1.† Compared to the reported single crystal unit cells of $Sn_2SbS_2I_3$ and $Sn_2SbSe_2I_3$, the determined unit cells for $Sn_2SbS_2I_3$ and Se substituted samples are in good agreement.[29] The Se substituted samples retain consistent a- and b-parameters, while a significant increase in c is observed, which is expected when comparing the pure S and Se analogs.[29]

To further ensure phase composition, energy dispersive X-ray spectroscopy (EDS) was performed. EDS reveals that although the bulk samples match the nominal stoichiometries quite well, there are secondary phases present (Fig. S2†). This may explain the abnormally high wR values of the Rietveld refinements in which some peak intensities are significantly different, despite factoring in possible preferred orientation (Fig. S1†). However, no possible overlapping binary or ternary phases (SnS, Sn_2S_3, Sn_2SI_2, *etc.*) could explain the difference in intensities, even based on measured EDS compositions. It is possible that the overlapping phase(s) could be related unidentified ternary or quaternary structures in this complex system.

3.3 Change in band gap

We characterized the optical band gap using diffuse reflectance spectroscopy. Fig. 3 shows an indirect bandgap of 1.64(2) eV for $Sn_2SbS_2I_3$, in good agreement with the 1.5 eV previously determined through photoconductivity measurements on a single crystal.[41] As Se substitution increases, a reduction of the bandgap to 1.60(2) eV and 1.55(2) eV are observed for $Sn_2SbS_{1.8}Se_{0.2}I_3$ and $Sn_2SbS_{1.5}Se_{0.5}I_3$, respectively (Fig. 3). This is consistent with physical inspection of the samples as the ground parent compound is a dark maroon colour which progresses to a brown-maroon colour at 0.2 Se, and even further into a gray-maroon colour at 0.5 Se. This also provides further evidence of successful substitution of S by Se.

This trend is contradictory to that observed when substituting Sn for Pb (increase in bandgap), but consistent with the substitution of Sb for Bi (decrease in bandgap) observed for related $Tt_2PnS_2I_3$ (Tt = Sn, Pb; Pn = Sb, Bi) compounds.[14] From an electronegativity standpoint, substitution of S for Se should shift the valence band energy higher and decrease the bandgap due to the lower electronegativity of Se, secondly, comparing the DFT relaxed structure with $Sn_2SbS_2I_3$ and $Sn_2SbSe_2I_3$, it is found that the difference between the two in structure mainly come from the components S(Se) and its nearest neighbours. Apart from the longer interatomic distance between S(Se) and Sn or Sb, their relative position is also distorted slightly. The change in bandgap is therefore due to both a change in electronegativity, as well as local structure, and both

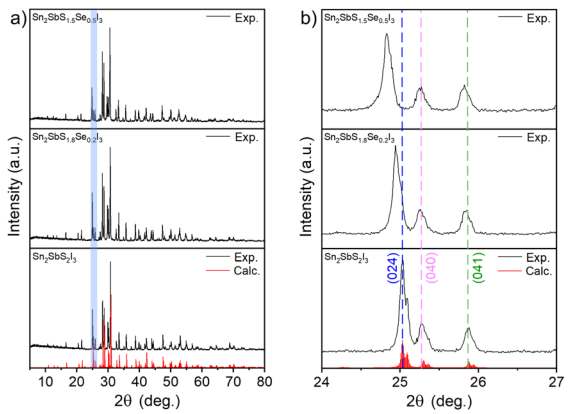

Fig. 2 Powder X-ray diffraction patterns of (a) the as synthesized $Sn_2SbS_{2-x}Se_xI_3$ ($x = 0$, 0.2, 0.5) samples and (b) zoomed in view of the blue highlighted section in (a) emphasizing observed peak shifts between samples. The calculated pattern for $Sn_2SbS_2I_3$ is shown in red for reference.[29]

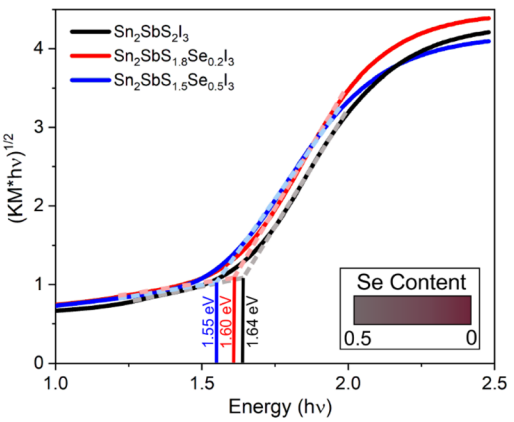

Fig. 3 Indirect bandgap Tauc plots of solid-state UV-vis Kubelka–Munk diffuse reflectance spectra for $Sn_2SbS_{2-x}Se_xI_3$ ($x = 0$, 0.2, 0.5). Colour gradient in the bottom right illustrates observed sample colours based on Se substitution amount.

affect the covalent part of bonding and thus the bandgap. Such an ability to fine tune the bandgap in this family of materials may be beneficial as $Pb_2SbS_2I_3$ was recently shown to be a robust material for solar cell applications.[42]

3.4 Thermal conductivity

Given the reported thermal conductivity of $Pb_2BiS_2I_3$ ranging between 0.7 and 1.2 W m^{-1} K^{-1} in the temperature range of 373–673 K, the related $Sn_2SbS_2I_3$ is expected to exhibit similarly low thermal conductivity.[14] Low thermal conductivities on the order of 0.5 W m^{-1} K^{-1} were also recently observed in the mixed anion compounds $MnSbS_2Cl$ and $MnBiS_2Cl$ which have similar elemental composition to the title compounds.[43] However, given the lighter elemental composition, thermal conductivity of $Sn_2SbS_2I_3$ is expected to be slightly higher to its Pb containing counterpart.

Thermal diffusivity measurements reveal exceptionally low thermal conductivity as low as 0.28 W m^{-1} K^{-1} for $Sn_2SbS_2I_3$ at 573 K (Fig. 4a). A further reduction of thermal conductivity is observed with the substitution of Se, achieving 0.22 W m^{-1} K^{-1} at 573 K for $Sn_2SbS_{1.5}Se_{0.5}I_3$ (Fig. 4a). This can be expected from the increase of structural disorder and phonon scattering from substitution and defects. The measured thermal conductivity shows a slight decrease with temperature for the parent sample but a very weak temperature dependence for the Se substituted samples. This suggests that phonon–phonon Umklapp scattering is so strong that the phonon mean free path reaches the amorphous limit, and the weakly temperature dependent coherent part of thermal conductivity plays an important role.[44]

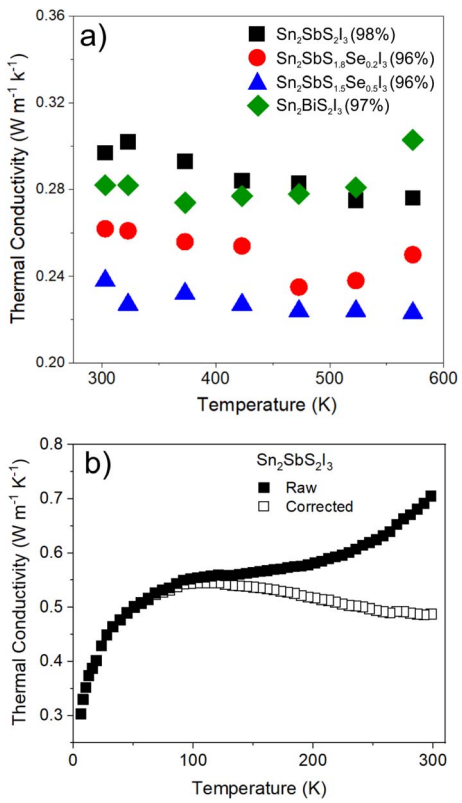

Fig. 4 (a) High temperature thermal conductivity of $Sn_2SbS_{2-x}Se_xI_3$ (x = 0, 0.2, 0.5) and $Sn_2BiS_2I_3$ with respective pellet densities and (b) low temperature thermal conductivity for $Sn_2SbS_2I_3$.

To confirm such unexpectedly low thermal conductivity measurements, we conducted two further experiments. First, we synthesized another member of the $Tt_2PnCh_2I_3$ (Tt = Sn, Pb; Pn = Sb, Bi; Ch = S, Se) family, namely $Sn_2BiS_2I_3$ for direct experimental comparison. Using an identical synthesis procedure used for $Sn_2SbS_2I_3$ similar purity product was confirmed through Rietveld refinement (Fig. S3†). Phase composition was confirmed through EDS and the optical bandgap matches well with previous reports (Fig. S4 and S5†).[14] Measured thermal conductivity for $Sn_2BiS_2I_3$ is shown in Fig. 4a and is of similar scale to $Sn_2SbS_2I_3$, suggesting this low thermal conductivity is not specific to the $Sn_2SbS_{2-x}Se_xI_3$ compositions, but can be observed in other members of the Sn containing family.

We also used a PPMS as a second method to measure thermal conductivity as a comparison. The thermal conductivity of the $Sn_2SbS_2I_3$ sample at low temperature is shown in Fig. 4b. Initially, an amorphous glass-like behaviour can be observed at low temperatures, however a T^4 dependence becomes dominant at higher temperatures. This suggests significant radiation loss during heating of the sample, which significantly skews thermal conductivity data above 150 K.[45] By applying a correction which accounts for additional radiative losses, the data collected above 150 K significantly changes and we observe a maximum value of thermal conductivity of about 0.54 W m^{-1} K^{-1} at around 100 K, which slowly decreases with further increase in temperature (see ESI† for detail of the postprocess correction method). After applying the correction, the measured thermal conductivity is approximately 0.49 W m^{-1} K^{-1}, at 300 K. While still exceptionally low this value is considerably larger than that observed through the LFA method. This inconsistency may come from the still existing underestimation of radiation loss, which is difficult to estimate correctly above 150 K and they are further enlarged by the non-optimal sample geometry (see Discussion in the ESI† for estimation of error in thermal conductivity measurements). Despite the possible errors in this temperature range, the important information revealed from the low temperature data is the absence of a well-defined Umklapp peak and that the thermal conductivity at low temperature cannot be described by the commonly used Debye model of lattice thermal conductivity including boundary scattering and phonon scattering, indicating that the assumptions used in the Debye model, such as the linear phonon dispersion and dominant acoustic phonon scattering are not sufficient to describe the actual case.[46,47] Nonetheless, the rounded thermal conductivity maximum and the rather weak temperature dependence suggests the early onset of strong phonon scattering from multiple sources.

Electrical property measurements of the samples proved unsuccessful using ZEM 2 and simple measurements with a multimeter were unable to produce readings, suggesting high resistivity. This is consistent with measurements done by Islam *et al.* on $Sn_2BiS_2I_3$ and $Pb_2SbS_2I_3$, which had resistivities above 1

MΩ.[14] The high resistivity indicates that the electronic contribution to the thermal conductivity is negligible and that the total thermal conductivity and lattice thermal conductivity are nearly identical.

3.5 First principles phonon calculation

Phonon dispersion was calculated for $Sn_2SbS_2I_3$ in the LT-$P2_1/c$ phase (structure as in Fig. 1d) using force constants from the displacement method. Typical features of phonon dispersion for heavy, multi-element compounds are present, namely, a low-lying acoustic phonon branch below 1 THz, and a low optical phonon frequency with most of the phonon modes concentrated near the 2 THz region, mainly from the I vibration, as can be seen from the phonon density of state in Fig. 5b. Higher frequency optical phonons mainly come from the motion of S. These are separate from the lower phonon bands and are unimportant for thermal transport.

Although defects, mixed and partial occupations that could be expected in experiment samples should play an important role in the ultralow thermal conductivity of current series of compounds, we do not attempt to cover their quantitative effects. Rather, we focus on the chemical reasoning through the anharmonicity of the structure, using Grüneisen parameter as an indicator. Grüneisen parameter is defined as the change in phonon frequency corresponding to cell expansion and is closely related to phonon anharmonicity.[48,49] The Grüneisen parameter of $Sn_2SbS_2I_3$ in the low frequency region is plotted in Fig. 5d. It is surprising to find the mode average Grüneisen parameter of all low frequency phonon (<1 THz) to be 2.44, with the highest value reaching over 5 for acoustic modes. This is on the same level with the calculated Grüneisen parameter of the strongly anharmonic SnSe (4.1, 2.1, 2.3 for *a*-, *b*-, and *c*-axis, respectively) and much larger in comparison with conventional thermoelectric compounds like PbTe (1.45).[50]

A microscopic picture of the anharmonicity is revealed by comparing the projected Grüneisen parameter of each atom, obtained by multiplying the mode Grüneisen parameter with the atomic component of phonon eigen-vectors, in the inset of Fig. 5d. From the projected Grüneisen parameter, it is found that Sn-involving phonon modes show high Grüneisen parameters. Fig. 5b also shows that Sn contributes to the largest phonon density of states in the lower frequency optical phonon region (0.5–1 THz). The phonon in these branches should scatter acoustic phonons effectively.[47,51,52] Therefore, we can conclude that Sn atoms are the most important source of the high anharmonicity we found in the structure and lead to a low thermal conductivity. This result also explains the low thermal conductivity of the Sn containing $Sn_2BiS_2I_3$ measured in the current work.

We attempt to establish the chemical reason for the high anharmonicity of the Sn atom from electronic structure calculation. Using the Bader's analysis method, we obtained the Bader's charge of each atoms Sn^{+1}, $Sb^{+1.85}$, $I^{-0.5}$ and $S^{-1.25}$.[53–55] Incomplete charge transfer for S and I, compared with their formal charge of −2 and −1 indicates covalent character, *i.e.*, the orbital components from Sn and Sb atoms are also important in the valence region. Indeed, the projected electronic density of state of $Sn_2SbS_2I_3$ in Fig. 5a and b shows the hybridization of p orbitals in the energy window from −5 to 0 eV. We would like to point out that some density of state from s orbital of Sn can be seen just below the valence band maximum. The s component can be identified to be anti-bonding since the main bonding region of Sn s orbital is

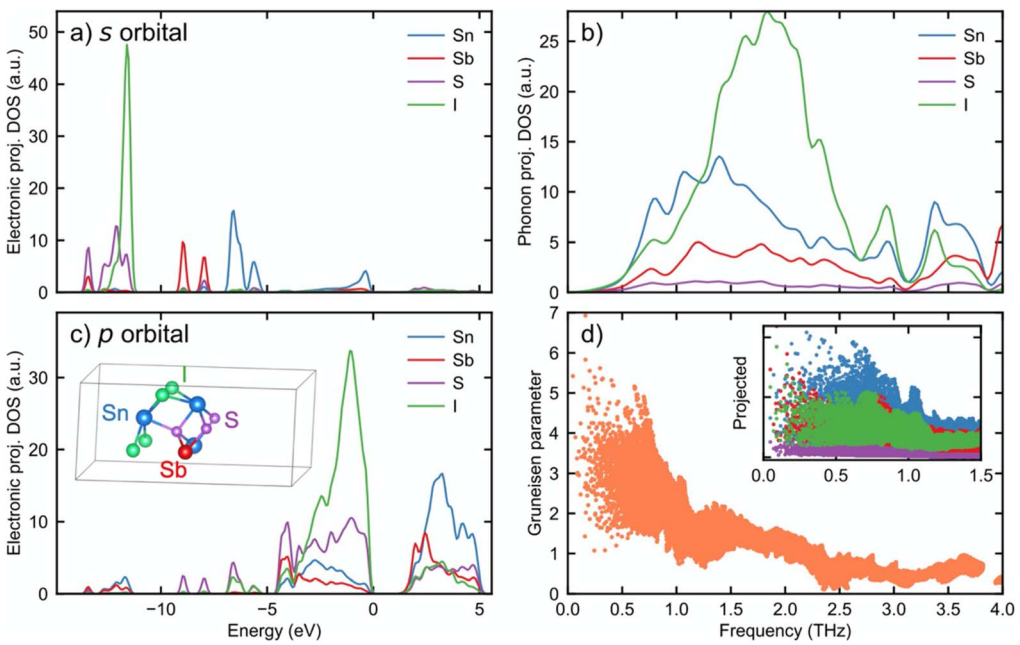

Fig. 5 (a) Projected s components of the electronic density of state for $Sn_2SbS_2I_3$ and (c) projected p components of the electronic density of state. (b) Projected phonon density of state onto different elements in the low frequency part and (d) Grüneisen parameter of each phonon mode sampled in the Brillouin zone. The inset in (d) projects Grüneisen parameter onto each atom with colours corresponding to (c).

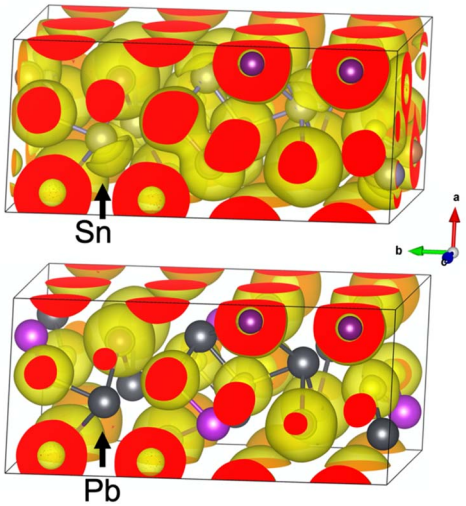

Fig. 6 Electron localization function ($\eta = 0.6$ surface) of the calculated LT-$P2_1/c$ structure of $Sn_2SbS_2I_3$, compared with that of $Pb_2BiS_2I_3$ counterpart. Sn and Pb atoms are pointed out using black arrows.

below −5 eV in energy as shown in projected density of states. This antibonding state would involve p orbital of Sn and S along their bonding direction due to the square pyramid like coordination of the Sn and stabilized due to the large interatomic space in the opposite side of S atom.[56]

The above anti-bonding Sn s component is exhibited in the electron localization function plotted in Fig. 6 with surface of ELF = 0.6.[53,57] The crescent moon shaped region near the Sn atom with high electron localization shows the antibonding states containing Sn s orbital in real space. Using integrated local density of state (ILDOS) from −2 to 0 eV, it can be shown that this electron localized region corresponds to the antibonding s orbital component discussed above (Fig. S9†). It is known that such "lone pair like" localized antibonding electronic states are important in suppressing lattice thermal conductivity as they introduce restoring force strongly deviated from harmonic approximation, thus leading to the large anharmonicity observed for Sn and the entire crystal structure of $Sn_2SbS_2I_3$.[58–61] In comparison, $Pb_2BiS_2I_3$ does not show strong localized antibonding states both in real space, as shown in Fig. 6 and in electronic density of states (Fig. S9†), highlighting the important role of the Sn antibonding s states in suppressing the lattice thermal conductivity.

4 Conclusions

The series $Sn_2SbS_{2-x}Se_xI_3$ (x = 0, 0.2, 0.5) was successfully synthesized and characterized by UV-vis diffuse reflectance spectroscopy and thermal diffusivity measurements, revealing a tunable band gap ranging from 1.55(2) to 1.64(2) eV and ultralow thermal conductivity in the range of 0.25 W m^{-1} K^{-1} from 303–573 K. Computational efforts elucidate the most stable crystal structure configuration of $Sn_2SbS_2I_3$ to be in a $P2_1/c$ configuration rather than the previously reported *Cmcm*. Further calculations using this model suggest that the ultralow thermal conductivity is attributed to the Sn atoms, which contribute largely to structural anharmonicity with localized antibonding s electrons. Such low thermal conductivity results for $Sn_2SbS_2I_3$ are counter-intuitive when compared to $Pb_2BiS_2I_3$ (0.7 W m^{-1} K^{-1}) suggesting that different electronic states can exist in the same family of compounds due to change in chemical composition and exploring such multicomponent systems can provide opportunity for rich chemistry and unique structure properties relationships.

Author contributions

Justin Mark: conceptualization, investigation (lead), data curation, formal analysis, visualization and draft preparation. Wenhao Zhang: data curation, investigation (calculation), formal analysis, visualization and draft preparation. Kazuhiko Maeda: review & editing. Takafumi Yamamoto: review & editing. Hiroshi Kageyama: review & editing. Takao Mori: conceptualization, funding acquisition, supervision, review & editing.

Conflicts of interest

There are no conflicts to declare.

Acknowledgements

This work was supported by JSPS KAKENHI JP16H06441, JP19H00833, JP22H05147, JP22H05148 and JST Mirai Program Grant Number JPMJMI19A1. We thank Prof. Jean-François Halet (CNRS-Saint-Gobain-NIMS) for the discussion on the chemical bonding.

References

1 J. K. Harada, N. Charles, K. R. Poeppelmeier and J. M. Rondinelli, *Adv. Mater.*, 2019, **31**, 1805295.
2 J. He, Z. Yao, V. I. Hegde, S. S. Naghavi, J. Shen, K. M. Bushick and C. Wolverton, *Chem. Mater.*, 2020, **32**, 8229–8242.
3 H. Kageyama, K. Hayashi, K. Maeda, J. P. Attfield, Z. Hiroi, J. M. Rondinelli and K. R. Poeppelmeier, *Nat. Commun.*, 2018, **9**, 772.
4 K. Maeda, F. Takeiri, G. Kobayashi, S. Matsuishi, H. Ogino, S. Ida, T. Mori, Y. Uchimoto, S. Tanabe, T. Hasegawa, N. Imanaka and H. Kageyama, *Bull. Chem. Soc. Jpn.*, 2022, **95**, 26–37.
5 J. Chen, C.-L. Hu, F.-F. Mao, J.-H. Feng and J.-G. Mao, *Angew. Chem., Int. Ed.*, 2019, **58**, 2098–2102.
6 B.-W. Liu, X.-M. Jiang, G.-E. Wang, H.-Y. Zeng, M.-J. Zhang, S.-F. Li, W.-H. Guo and G.-C. Guo, *Chem. Mater.*, 2015, **27**, 8189–8192.
7 W. Xing, P. Fang, N. Wang, Z. Li, Z. Lin, J. Yao, W. Yin and B. Kang, *Inorg. Chem.*, 2020, **59**, 16716–16724.
8 W. S. Tang, K. Yoshida, A. V. Soloninin, R. V. Skoryunov, O. A. Babanova, A. V. Skripov, M. Dimitrievska, V. Stavila, S. Orimo and T. J. Udovic, *ACS Energy Lett.*, 2016, **1**, 659–664.

9 F. Li, J.-F. Li, L.-D. Zhao, K. Xiang, Y. Liu, B.-P. Zhang, Y.-H. Lin, C.-W. Nan and H.-M. Zhu, *Energy Environ. Sci.*, 2012, **5**, 7188.
10 J. Li, J. Sui, Y. Pei, C. Barreteau, D. Berardan, N. Dragoe, W. Cai, J. He and L.-D. Zhao, *Energy Environ. Sci.*, 2012, **5**, 8543.
11 Y. Liu, L.-D. Zhao, Y. Liu, J. Lan, W. Xu, F. Li, B.-P. Zhang, D. Berardan, N. Dragoe, Y.-H. Lin, C.-W. Nan, J.-F. Li and H. Zhu, *J. Am. Chem. Soc.*, 2011, **133**, 20112–20115.
12 L.-D. Zhao, J. He, D. Berardan, Y. Lin, J.-F. Li, C.-W. Nan and N. Dragoe, *Energy Environ. Sci.*, 2014, **7**, 2900–2924.
13 M. Amsler, L. Ward, V. I. Hegde, M. G. Goesten, X. Yi and C. Wolverton, *Phys. Rev. Mater.*, 2019, **3**, 035404.
14 S. M. Islam, C. D. Malliakas, D. Sarma, D. C. Maloney, C. C. Stoumpos, O. Y. Kontsevoi, A. J. Freeman and M. G. Kanatzidis, *Chem. Mater.*, 2016, **28**, 7332–7343.
15 Q. D. Gibson, T. Zhao, L. M. Daniels, H. C. Walker, R. Daou, S. Hébert, M. Zanella, M. S. Dyer, J. B. Claridge, B. Slater, M. W. Gaultois, F. Corà, J. Alaria and M. J. Rosseinsky, *Science*, 2021, **373**, 1017–1022.
16 K. Biswas, J. He, I. D. Blum, C.-I. Wu, T. P. Hogan, D. N. Seidman, V. P. Dravid and M. G. Kanatzidis, *Nature*, 2012, **489**, 414–418.
17 J. Mao, Z. Liu, J. Zhou, H. Zhu, Q. Zhang, G. Chen and Z. Ren, *Adv. Phys.*, 2018, **67**, 69–147.
18 Z. Liu, W. Gao, H. Oshima, K. Nagase, C.-H. Lee and T. Mori, *Nat. Commun.*, 2022, **13**, 1120.
19 X. Zhou, G. Wang, L. Zhang, H. Chi, X. Su, J. Sakamoto and C. Uher, *J. Mater. Chem.*, 2012, **22**, 2958–2964.
20 Z. Liu, J. Mao, T.-H. Liu, G. Chen and Z. Ren, *MRS Bull.*, 2018, **43**, 181–186.
21 Y. Jiang, J. Dong, H.-L. Zhuang, J. Yu, B. Su, H. Li, J. Pei, F.-H. Sun, M. Zhou, H. Hu, J.-W. Li, Z. Han, B.-P. Zhang, T. Mori and J.-F. Li, *Nat. Commun.*, 2022, **13**, 6087.
22 Z. Liu, N. Sato, W. Gao, K. Yubuta, N. Kawamoto, M. Mitome, K. Kurashima, Y. Owada, K. Nagase, C.-H. Lee, J. Yi, K. Tsuchiya and T. Mori, *Joule*, 2021, **5**, 1196–1208.
23 J. M. Ziman, *Electrons and Phonons: The Theory of Transport Phenomena in Solids*, Clarendon Press, Oxford University Press, Oxford: New York, 2001.
24 Z. Liu and T. Mori, in *System-Materials Nanoarchitectonics*, ed. Y. Wakayama and K. Ariga, Springer, Japan, Tokyo, 2022, pp. 199–231.
25 Z. Liu, W. Zhang, W. Gao and T. Mori, *Energy Environ. Sci.*, 2021, **14**, 3579–3587.
26 E. S. Toberer, A. Zevalkink and G. J. Snyder, *J. Mater. Chem.*, 2011, **21**, 15843.
27 G. A. Slack, *Semiconductors and Semimetals*, Academic Press, New York, 1979, vol. 34.
28 C. Doussier, Y. Moëlo, P. Léone, A. Meerschaut and M. Evain, *Solid State Sci.*, 2007, **9**, 792–803.
29 A. Ibanez, J.-C. Jumas, J. Olivier-Fourcade and E. Philippot, *J. Solid State Chem.*, 1984, **55**, 83–91.
30 J. Olivier-Fourcade, J. C. Jumas, M. Maurin and E. Philippot, *Z. Anorg. Allg. Chem.*, 1980, **468**, 91–98.
31 K. Ogawa, H. Suzuki, C. Zhong, R. Sakamoto, O. Tomita, A. Saeki, H. Kageyama and R. Abe, *J. Am. Chem. Soc.*, 2021, **143**, 8446–8453.
32 B. H. Toby and R. B. Von Dreele, *J. Appl. Crystallogr.*, 2013, **46**, 544–549.
33 P. Giannozzi, S. Baroni, N. Bonini, M. Calandra, R. Car, C. Cavazzoni, D. Ceresoli, G. L. Chiarotti, M. Cococcioni, I. Dabo, A. Dal Corso, S. de Gironcoli, S. Fabris, G. Fratesi, R. Gebauer, U. Gerstmann, C. Gougoussis, A. Kokalj, M. Lazzeri, L. Martin-Samos, N. Marzari, F. Mauri, R. Mazzarello, S. Paolini, A. Pasquarello, L. Paulatto, C. Sbraccia, S. Scandolo, G. Sclauzero, A. P. Seitsonen, A. Smogunov, P. Umari and R. M. Wentzcovitch, *J. Phys.: Condens. Matter*, 2009, **21**, 395502.
34 P. E. Blöchl, *Phys. Rev. B: Condens. Matter Mater. Phys.*, 1994, **50**, 17953–17979.
35 J. P. Perdew, K. Burke and M. Ernzerhof, *Phys. Rev. Lett.*, 1996, **77**, 3865–3868.
36 M. Dion, H. Rydberg, E. Schröder, D. C. Langreth and B. I. Lundqvist, *Phys. Rev. Lett.*, 2004, **92**, 246401.
37 W. Tang, E. Sanville and G. Henkelman, *J. Phys.: Condens. Matter*, 2009, **21**, 084204.
38 A. Togo and I. Tanaka, *Scr. Mater.*, 2015, **108**, 1–5.
39 M. I. Aroyo, D. Orobengoa, G. de la Flor, E. S. Tasci, J. M. Perez-Mato and H. Wondratschek, *Acta Crystallogr., Sect. A: Found. Adv.*, 2014, **70**, 126–137.
40 E. Kroumova, J. M. Perez-Mato and M. I. Aroyo, *J. Appl. Crystallogr.*, 1998, **31**, 646.
41 V. I. Starosta, J. Kroutil and L. Beneš, *Cryst. Res. Technol.*, 1990, **25**, 1439–1442.
42 R. Nie, B. Kim, S.-T. Hong and S. I. Seok, *ACS Energy Lett.*, 2018, **3**, 2376–2382.
43 N. Sato, N. Kuroda, S. Nakamura, Y. Katsura, I. Kanazawa, K. Kimura and T. Mori, *J. Mater. Chem. A*, 2021, **9**, 22660–22669.
44 M. Simoncelli, N. Marzari and F. Mauri, *Nat. Phys.*, 2019, **15**, 809–813.
45 A. L. Pope, B. Zawilski and T. M. Tritt, *Cryogenics*, 2001, **41**, 725–731.
46 J. Yang, G. P. Meisner, D. T. Morelli and C. Uher, *Phys. Rev. B: Condens. Matter Mater. Phys.*, 2000, **63**, 014410.
47 S. Misra, C. Barreteau, J.-C. Crivello, V. M. Giordano, J.-P. Castellan, Y. Sidis, P. Levinský, J. Hejtmánek, B. Malaman, A. Dauscher, B. Lenoir, C. Candolfi and S. Pailhès, *Phys. Rev. Res.*, 2020, **2**, 043371.
48 N. W. Ashcroft and N. D. Mermin, *Solid State Physics*, Holt, Rinehart and Winston, New York, 1976.
49 C. H. Lee and C. K. Gan, *Phys. Rev. B*, 2017, **96**, 035105.
50 L.-D. Zhao, S.-H. Lo, Y. Zhang, H. Sun, G. Tan, C. Uher, C. Wolverton, V. P. Dravid and M. G. Kanatzidis, *Nature*, 2014, **508**, 373–377.
51 W. Li, J. Carrete, G. K. H. Madsen and N. Mingo, *Phys. Rev. B*, 2016, **93**, 205203.
52 M. M. Koza, M. R. Johnson, R. Viennois, H. Mutka, L. Girard and D. Ravot, *Nat. Mater.*, 2008, **7**, 805–810.
53 G. Frenking, *The Chemical Bond*, Wiley-VCH, Weinheim, 2014.

54 R. F. W. Bader, *Chem. Rev.*, 1991, **91**, 893–928.
55 P. S. V. Kumar, V. Raghavendra and V. Subramanian, *J. Chem. Sci.*, 2016, **128**, 1527–1536.
56 T. A. Albright, J. K. Burdett and M.-H. Whangbo, *Orbital Interactions in Chemistry*, Wiley, Hoboken, New Jersey, 2nd edn, 2013.
57 A. Savin, R. Nesper, S. Wengert and T. F. Fässler, *Angew. Chem., Int. Ed. Engl.*, 1997, **36**, 1808–1832.
58 O. Cherniushok, R. Cardoso-Gil, T. Parashchuk, R. Knura, Y. Grin and K. T. Wojciechowski, *Chem. Mater.*, 2022, **34**, 6389–6401.
59 M. D. Nielsen, V. Ozolins and J. P. Heremans, *Energy Environ. Sci.*, 2013, **6**, 570–578.
60 E. J. Skoug and D. T. Morelli, *Phys. Rev. Lett.*, 2011, **107**, 235901.
61 W. Zhang, N. Sato, K. Tobita, K. Kimura and T. Mori, *Chem. Mater.*, 2020, **32**, 5335–5342.